

Identifying the Microtearing Modes in the pedestal of DIII-D H-modes using Gyrokinetic Simulations

Ehab Hassan*

*Oak Ridge National Laboratory, TN, US
Institute for Fusion Studies, University of Texas at Austin, Austin, TX, US and
Physics, Faculty of Science, Ain Shams University, Cairo 11566, Egypt*

D.R. Hatch, M.R. Halfmoon, M. Curie, M.T. Kotchenreuther, and S.M. Mahajan
Institute for Fusion Studies, University of Texas at Austin, Austin, TX, US

G. Merlo

Oden Institute, University of Texas at Austin, Austin, TX, US

R.J. Groebner

General Atomics, San Diego, CA, US

A.O. Nelson

Columbia University, NY, US

A. Diallo

Princeton Plasma Physics Laboratory, NJ, US

(Dated: December 23, 2021)

Recent evidence points toward the microtearing mode (MTM) as an important fluctuation in the H-mode pedestal for anomalous electron heat transport. A study of the instabilities in the pedestal region carried out using gyrokinetic simulations to model an ELMy H-mode DIII-D discharge (USN configuration, 1.4 MA plasma current, and 3 MW heating power) is presented. The simulations produce MTMs, identified by predominantly electromagnetic heat flux, small particle flux, and a substantial degree of tearing parity. The magnetic spectrogram from Mirnov coils exhibits three distinct frequency bands—two narrow bands at lower frequency (~ 35 -55 kHz and ~ 70 -105 kHz) and a broader band at higher frequency (~ 300 -500 kHz). Global linear GENE simulations produce MTMs that are centered at the peak of the ω_* profile and correspond closely with the bands in the spectrogram. The three distinctive frequency bands can be understood from the basic physical mechanisms underlying the instabilities. For example (i) instability of certain toroidal mode numbers (n) is controlled by the alignment of their rational surfaces with the peak in the ω_* profile, and (ii) MTM instabilities in the lower n bands are the conventional collisional slab MTM, whereas the higher n band depends on curvature drive. While many features of the modes can be captured with the local approximation, a global treatment is necessary to quantitatively reproduce the detailed band gaps of the low- n fluctuations. Notably, the transport signatures of the MTM are consistent with careful edge modeling by SOLPS.

NOTICE OF COPYRIGHT: This manuscript has been authored in part by UT-Battelle, LLC, under contract DE-AC05-00OR22725 with the US Department of Energy (DOE). The US government retains and the publisher, by accepting the article for publication, acknowledges that the US government retains a nonexclusive, paid-up, irrevocable, worldwide license to publish or reproduce the published form of this manuscript, or allow others to do so, for US government purposes. DOE will provide public access to these results of federally sponsored research in accordance with the DOE Public Access Plan (<http://energy.gov/downloads/doe-public-access-plan>).

I. INTRODUCTION

This paper reports on a gyrokinetic study of microtearing modes (MTMs) in the DIII-D pedestal. We describe careful comparisons with magnetic fluctuation data and elucidate the physics underlying the distinctive features of experimental frequency spectrum.

The MTM is an electromagnetic microinstability dominated by electron dynamics at ion length scales. The resulting

fluctuations are characterized by their large magnetic component, distinctive frequency ($\omega \sim \omega_*$), and large heat transport in the electron channel via magnetic flutter. While the conventional tearing modes are driven by current gradients, the essential drive of the MTM is the electron temperature gradient. The earliest work showed that a finite collision frequency comparable to ω_* was necessary to stimulate the MTM in both the slab (Ref. 1) and cylindrical (Ref. 2) geometries.

The crossover of electrons near the trapped-passing boundary is required to enhance the collision rates in the low collisionality regimes and destabilize the MTMs (Ref. 3). Thus, it was posited that MTMs are stable in collisionless regimes

* hassanem@ornl.gov

and, perhaps, less relevant for tokamaks with large aspect ratio operating at the high temperatures ($v \ll \omega_*$) relevant for a reactor. Consequently, many earlier studies of MTM have focused on spherical tokamaks (Ref. 4–8).

Interest in MTM has been vigorously revived for standard aspect ratio tokamaks such as discussed in 9 and 10. In particular, a series of recent papers has demonstrated that MTM is a prominent fluctuation in the steep gradient region of the pedestal (Ref. 11–13). Hatch et al. 11 identified MTM as the salient ion-scale instability in a JET ITER-like wall (JET-ILW) discharge, noted its unusual mode structure (peaking at the top and bottom of the tokamak), and demonstrated that nonlinear simulations can reproduce experimental transport levels. Kotschenreuther et al. 12 outlined fundamental physical arguments for the likelihood of MTMs as an important pedestal fluctuation and made direct connections between GK simulations and magnetic spectrograms for two DIII-D discharges. Recently, Hatch et al. 13 demonstrated quantitative agreement between gyrokinetic simulations and magnetic spectrograms from JET and explained the distinctive frequency bands by the alignment of certain rational surfaces with the peak in the profile of the diamagnetic frequency ω_* . More generally, the recent DOE-FES theory performance target (of which this work was a part), surveyed a broad range of discharges spanning several devices and modes of operation and identified MTM in nearly all ELMy H-modes examined as shown in 14 and 15. In addition to the pedestal observations, Jian et al. 16 identifies MTM in an internal transport barrier on DIII-D, suggesting that MTM are not limited solely to edge transport barriers, but, rather, may be a common feature of transport barriers in general.

Recently, innovative experimental diagnostics of internal magnetic fluctuations (Ref. 17) have further established MTM as a common pedestal fluctuation in DIII-D as discussed in 18 and 19. Related gyrokinetic modeling will be reported in 20. Collectively, these results suggest that MTMs are likely responsible for many of the most prominent magnetic fluctuations observed in the pedestal of tokamaks (see Ref. 18, 21–26).

The experimental findings from the DIII-D discharge 162940 are detailed in section II, and the use of the plasma profiles and equilibrium of that discharge to examine the possibility for finding signatures for the MTMs is reported in section III. Afterward, the results of the local and global linear gyrokinetic simulations are presented and discussed in section IV. Section V shows the MTM structures with elaboration on different physics mechanisms that are responsible for destabilizing the MTM. Local nonlinear simulations are described in section VI. Finally, conclusions and acknowledgements are listed in sections VII and VIII.

II. DIII-D DISCHARGE 162940

DIII-D discharge 162940 was part of an experiment that measures the effect of divertor closure on the pedestal density profile, detachment onset, and heat flux control (Ref. 27). This discharge is in an upper-single-null (USN) configuration

with the ion $\mathbf{B} \times \nabla \mathbf{B}$ drift towards the X-point and is entirely beam-heated with ~ 3 MW of modulated beam power throughout. Importantly, the discharge has a low (~ 15 Hz) and consistent ELM frequency around the chosen time slice. The slow ELM frequency allows for the detailed gyrokinetic studies presented in this paper by increasing data resolution between ELMs, where 80–99% of the phase of the ELM cycle was used to construct this equilibrium. The end of the ELM cycle represents the period with steepest temperature gradients and saturated temperature profiles. Consequently, it is expected that the instabilities are most robustly unstable—and most easily identified—during this period.

The measured thermal pressure profile, the computed beam pressure profile and the edge neoclassical bootstrap current model, as well as the temperature and density profiles, were used to construct the "kinetic" equilibrium for the DIII-D discharge 162940, and they show clear signatures of an H-mode operation for this discharge. The workflow that followed uses an extra iteration after the initial kinetic equilibrium is made to re-map all of the experimental data onto the new EFIT of higher resolution, i.e. 513×513 , and then to recompute the equilibrium with the re-mapped temperature and density profiles. This improves the self-consistency between the profiles and the equilibrium. This plasma is strongly shaped with an elongation of 1.78 and upper and lower triangularities of 0.71 and 0.28, respectively.

The magnetic spectrogram for DIII-D discharge 162940 is shown in Fig. (1). For the present study, three lab frame frequency bands are of interest: $f \sim 35 - 55$ kHz, $f \sim 70 - 105$ kHz, and $f \sim 300 - 500$ kHz. These quasi-coherent fluctuations are denoted with magenta lines in Fig. (1). From Fourier analysis of fast magnetic measurements, the toroidal mode number n was determined to be $n = 3$ for the lowest frequency ($f = 35 - 55$ kHz) mode (28). As shown below, gyrokinetic simulations agree with this measurement. Resolution on the magnetic diagnostics is not high enough to experimentally determine the n number for the two high-frequency bands. These bands are correlated with the inter-ELM cycle and such bands have been shown elsewhere to be localized in or near the pedestal (see Refs. 23 and 24). Most other frequency signatures are only weakly correlated with the ELM cycle and are likely core fluctuations. Here we seek to answer the questions: (i) what is the instability underlying these quasi-coherent pedestal fluctuations, and (ii) what is the physical mechanism underlying the distinctive band structure?

III. PRELIMINARY CONSIDERATIONS: INITIAL PROFILE PREDICTIONS

Useful insights can be gained from a simple examination of the MTM frequency in the pedestal. The MTM frequency is closely tied to $\omega^* = k_y \rho_s c_s (1/L_{n_e} + 1/L_{T_e})$, where k_y is the wavenumber, ρ_s is the gyroradius, c_s is the ion acoustic speed, L_{n_e} is the electron density gradient scale-length, and L_{T_e} is the electron temperature gradient scale-length. Due to the rapidly changing (in the radial direction) profiles in the pedestal, however, this knowledge is only useful if we know the relevant ra-

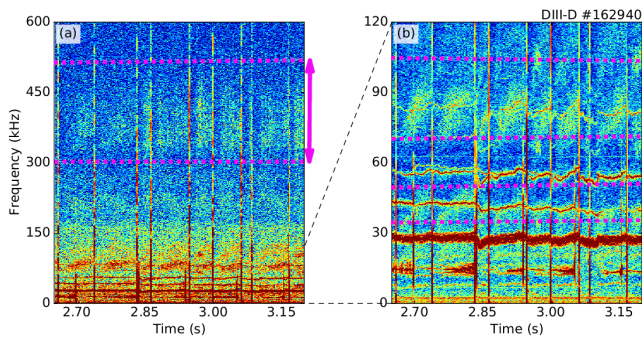


FIG. 1. A spectrogram of magnetic fluctuations observed in signals from Mirnov coils for the DIII-D discharge #162940 from 2.85s to 3.15s. The vertical lines correspond to ELMS. The fluctuations of interest are those that correlate with the ELM-cycle—i.e. fluctuation bands that are weak (or vanishing) immediately after the ELM and then have upward-sweeping frequencies as the pedestal gradients recover. These quasi-coherent fluctuation bands are highlighted in magenta. Note that, at lower frequencies, core modes that are weakly (or un-) correlated with the ELM cycle are also manifest.

dial localization of the fluctuation. Ref. 13 shows that pedestal MTMs localize at the peak of the ω^* profile and can only result in instability if this peak aligns with the relevant rational surface for a given toroidal mode number n . This information allows a preliminary survey of the fluctuations even before resorting to gyrokinetic simulations.

Fig. (2) illustrates these considerations. In this figure, the curves show the diamagnetic frequencies in the lab frame, $\omega^* + \omega_D$, where ω_D is the Doppler Shift, for a range of toroidal mode numbers $n = 2 - 6$. The frequency bands from the spectrogram are shown in orange and the vertical lines denote rational surfaces $q = m/n$ for various combinations of n and poloidal mode number m . The particular values of m in fig. 2 are chosen such that the rational surface m/n lies closest to the peak of the ω^* profile.

Several toroidal mode numbers ($n = 3, 5, 6$) correspond to rational surface near the peak of ω^* and have diamagnetic frequencies (shown in green) that fall within (or near) the observed frequency range. This suggests that the corresponding toroidal mode numbers may have unstable MTMs and are good candidates to explain the observed fluctuations. Note here that one of the rational surfaces in alignment with the lowest frequency band agrees with the experimental measurement of $n = 3$. On the other hand and although the red curves (diamagnetic frequencies for $n = 2, 4$) fall near the observed bands, their corresponding rational surfaces are located far from the peak of the diamagnetic frequency (ω^*) profile for each mode and we would thus expect these modes to be stable. In contrast the rational surfaces of the modes at $n = 3, 5, 6$ lie at or close to the peak of the ω^* profile. As we will show below in Sec. IV, these predictions are borne out in gyrokinetic simulations. We note that the frequencies for the unstable toroidal mode numbers $n = 3, 5, 6$ lie at the higher end of the observed frequency bands. This was also observed in Refs. 12 and 13, where it was explained by localized flattening of background profiles in the nonlinear state.

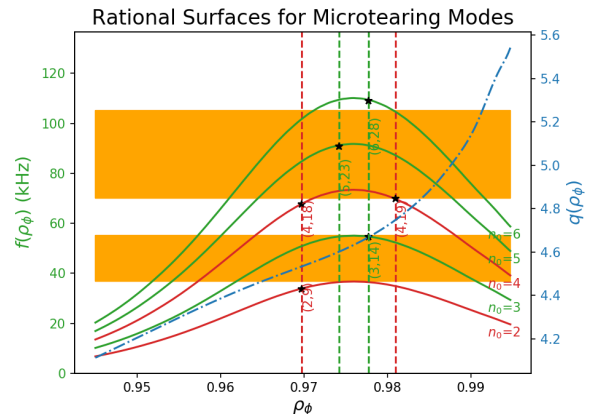


FIG. 2. The lab-frame diamagnetic frequency profile over the pedestal region for a selected toroidal mode number (2 – 6) in green or red. The orange frequency band are corresponding to the frequency of the magnetic fluctuations measured experimentally by the Mirnov coils. The vertical lines are the rational surfaces corresponding to each mode number, and the blue line represents the safety factor.

For the purposes of this paper, we note two considerations regarding the localization of the modes near the peak in ω^* and the consequent sensitive selection of unstable n numbers.

1. The first consideration is very simple. A mode is most likely to be unstable at the location where its drive is maximized, in this case, the peak of the ω^* profile.
2. A more comprehensive answer requires a detailed study of the global eigenmode problem. More specifically, a global MTM eigenmode depends on the cooperation of the standard “potential well” created by magnetic shear as well as the variation of ω^* . The proximity of the rational surface near the ω^* peak seems to reinforce the potential well. This is currently under investigation and will be published elsewhere.

These considerations have been studied in detail and reported in a separate publication, which concludes that the latter mechanism is in effect (Ref. 29).

Having made these preliminary investigations, we move now to gyrokinetic simulations.

IV. GYROKINETIC SIMULATIONS

The main questions of interest are: (i) what instabilities are responsible for the magnetic fluctuations, and (ii) what is the underlying physical mechanism responsible for the distinctive band structure? As will become clear below, we are able to answer these questions rather conclusively using linear gyrokinetic simulations.

A series of global and local linear simulations have been carried out using the GENE gyrokinetic code (Refs. 30 and 31) to examine the presence and role of MTMs in the DIII-D discharge 162940.

We consider both local and global treatments. The two approaches are qualitatively similar, although a global treatment is necessary to recover the banded structure at lower frequencies. While the global simulations span the pedestal, the local simulations examine three locations near the peak of the ω_* profiles, i.e. $\rho_\phi = 0.965, 0.970,$ and 0.975 .

A. Local Linear Simulations

A series of local linear simulations is carried out over a range of toroidal mode numbers ($n = 1 - 30$) at three radial locations $\rho_\phi = 0.965, 0.970,$ and 0.975 . Here we include three-species (deuterium, electrons and carbon) and employ the Landau collision operator. Convergence tests show that the following resolution is sufficient to resolve the instabilities: $n_x=16, n_z=160, n_v=48,$ and $n_w=24$ in the radial wavenumber (k_x), parallel (z), parallel velocity v_{\parallel} and magnetic moment μ coordinates, respectively. The electron density and temperature, along with their inverse gradient scale lengths, in addition to the collision frequency ($\nu_{ei} = n_0 e^4 \pi \ln \Lambda / \sqrt{m_e T_{e0}^3 / 2}$), magnetic shear ($\hat{s} = r L_q$), safety factor (q), and beta ($\beta = (n_e k_B T_e) / (B^2 / 2 \mu_0)$) values at the selected locations are shown in table(I):

TABLE I. Profile parameters for local linear simulations

Parameter	$\rho_\phi=0.965$	$\rho_\phi=0.970$	$\rho_\phi=0.975$
$n_e (10^{19})$	4.93	4.43	3.84
$T_e (keV)$	0.468	0.403	0.331
a/L_{n_e}	17.93	24.7061	32.02133
a/L_{T_e}	25.73	34.46	44.05
ν_N	5.74×10^{-3}	6.91×10^{-3}	8.80×10^{-3}
β	2.26×10^{-3}	1.75×10^{-3}	1.25×10^{-3}
\hat{s}	3.25	3.05	3.65
q	4.46	4.53	4.61

The mode frequencies in Fig. 3 are clearly in the electron diamagnetic direction and close to ω_* as expected for MTM. The frequency of the unstable modes is monotonically increasing with the radial locations (ρ_ϕ) and the mode numbers (n_ϕ) in both the lower and upper bands. The growth rates, on the other hand, show different profiles in the lower and upper bands.

Further characteristics of the modes are shown in Fig. 4, where we plot the ratio between (i) the electromagnetic and electrostatic components of the heat flux (Q_{em}/Q_{es}), (ii) the ion and electron heat diffusivities (χ_i/χ_e), and (iii) the electron particle diffusivity to the electron heat diffusivity (D_e/χ_e). Heat (χ_s) and particle (D_s) transport diffusivity for each species (s) are defined as the particle (Γ_s) and/or heat (Q_s) fluxes multiplied by the gradient scale-length (L_{n_s} or L_{T_s}), where:

$$D_s = L_{n_s} \Gamma_s / n_s$$

$$\chi_s = L_{T_s} [Q_s - (3/2) T_s \Gamma_s] / n_s T_s$$

where the particle and heat fluxes are calculated inside GENE code and provided as an output. The formulas for these fluxes

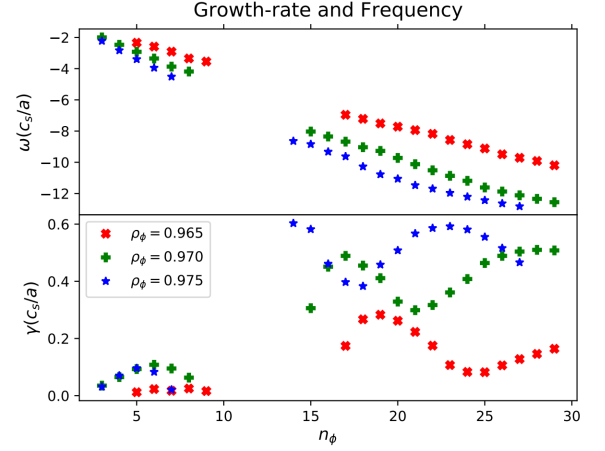


FIG. 3. The angular frequency (top) and growth rates from a set of local linear simulations scan over a range of toroidal mode numbers ($n_\phi = 3 - 29$) at three different locations ($\rho_\phi = 0.965$ (red), 0.970 (green), and 0.975 (blue)).

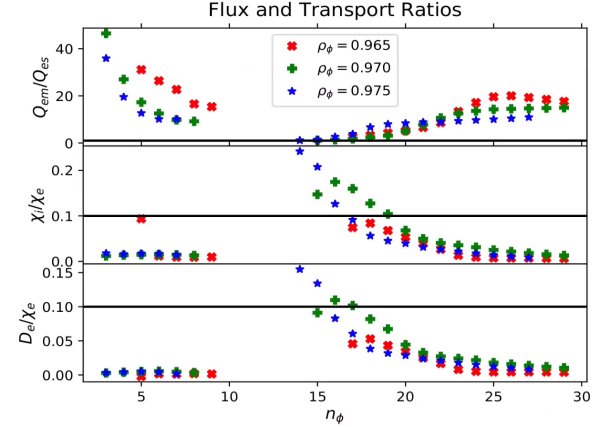


FIG. 4. The ratio of the electromagnetic-to-electrostatic heat flux (top), the ion-to-electron heat transport (middle), and the heat-to-particle transport of the electrons (bottom) for a local linear simulation scan over a range of toroidal mode numbers ($n_\phi = 3 - 29$) at three different locations ($\rho_\phi = 0.965$ (red), 0.970 (green), and 0.975 (blue)).

are standard and reported in, e.g., Ref. 32.

The dominance of the electromagnetic component of the heat flux (Q_{em}) is a clear signature of MTM. The other ratios are also consistent with ETG.

The diffusivity ratios shown in Fig. 4 (and below in Fig. 5) are of particular interest. The DIII-D discharge studied here was the also the focus of a successful SOLPS-UEDGE benchmarking exercise as well as extensive sensitivity tests carried out with SOLPS Ref. 14. The results from these studies show that the conclusion that $D_e/\chi_e \ll 1$ is not only in force for this discharge, but typical of the pedestals in general, indicating that a substantial heat transport mechanism is required in addition to any MHD instabilities (like KBM) that may be active (Ref. 12). The MTM is an eminently suitable candidate

as indicated by the diffusivity ratios reported here.

The transport ratios shown in Fig. 4 exhibit two distinct regions of unstable modes (instead of the three distinct bands shown in the spectrogram in Fig. 1), with the lower region extending from $n = 2 - 9$ and the upper region extending from $n = 15 - 29$ for the three selected locations. This already captures some features of the spectrogram, namely the cluster of fluctuations at low frequencies and a separate broad band at high frequencies. However, these local linear results are not consistent with the distinct low frequency bands ($f < 100$ kHz) since the modes are unstable at each consecutive n number. As will be shown below, a global treatment is required to reproduce this phenomenon.

Although the transport ratios are consistent with MTM in all cases, the relative magnitudes of the ratios are quite different between the two bands. This suggests there may be two different branches of MTM, as will be further explored below.

B. Global Linear Simulations

While the local linear simulations were able to identify the unstable MTM modes in two distinct bands, they failed to reproduce the structure of the low frequency bands (below 105 kHz). As it turns out, global effects are necessary to reproduce the low- n behavior, as described in this section.

Global linear simulations are centered at the middle of the pedestal $\rho_\phi = 0.970$ and span the steep gradient region of the pedestal (radial domain $\rho_\phi = 0.9425 - 0.9975$). Buffer zones (~ 0.1) are employed at each end of the box to ease the transition to the Dirichlet boundary condition at each end with upper/lower Krook coefficient of ~ 1 . To identify the required resolution, a convergence test was carried out at two mode numbers, one in the lower band ($n=5$) and another one in the upper band ($n=20$). This convergence test shows that the unstable MTMs are resolved with the following set of grid resolution: $n_x=120$, $n_z=90$, $n_v=48$, and $n_w=24$, where n_x is the number of radial grid points, and n_z , n_v , and n_w are defined in subsection IV A. The global linear simulations benefited from using block structured grids, which adapt the velocity space box to the local, where l_v and l_w are set to 3.13 and 11.86, respectively (see Refs. 33 and 34). This allows the grid resolutions in the velocity space (v and w) to match the local requirements.

The transport ratios of the globally unstable modes are shown in Fig. 5. The ratio of the electron to ion heat transport ratios, χ_e/χ_i , (red crosses) and the heat to particle transport ratios, χ_e/D_e , (green pluses) for the electrons are found to be much greater than 10. This suggests classification as ETG or MTM. However, the dominance of the electromagnetic heat flux, Q_{em} , (blue diamonds) over the electrostatic heat flux, Q_{es} clearly indicates MTM. Once again, while there is considerable variation between the regions (e.g. the electromagnetic nature is clearly stronger for the low n region), all signatures are consistent with MTM. Although the global results are qualitatively similar to the local results, the ratios χ_i/χ_e and D_e/χ_e are much smaller in the global linear simulations.

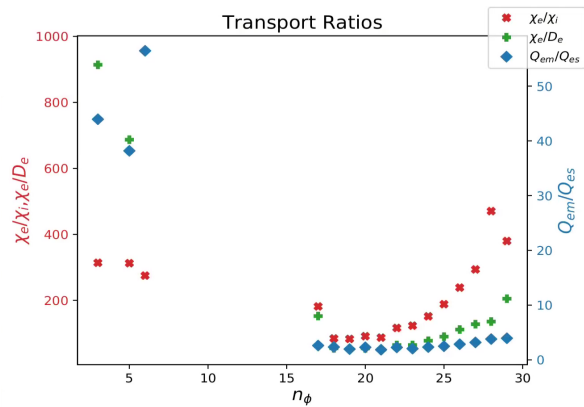


FIG. 5. The ratio of the electromagnetic-to-electrostatic heat flux (blue), the electron-to-ion heat transport (red), and the heat-to-particle transport (green) of the electrons for a global linear simulation scan over a range of toroidal mode numbers ($n_\phi = 3 - 29$).

Similar to the results from the local linear simulations, the ratio of the heat transport of electrons to ions is equivalent to the lower and upper bands, however the electron particle transport is much smaller than the electron heat transport in the lower band compared to the upper band. The linear

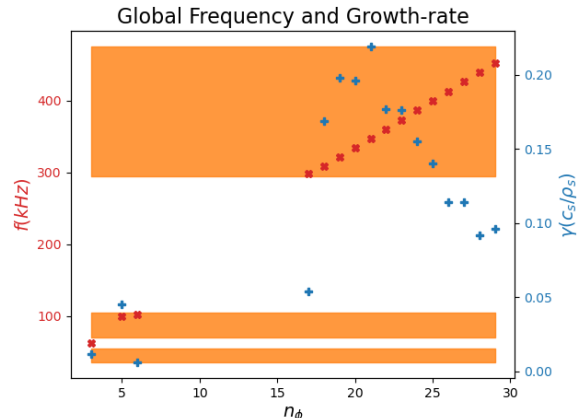


FIG. 6. The comparison between the unstable modes frequencies (in SI units) in (red crosses) and the frequency of the magnetic fluctuations measured experimentally (green bands) shows that the global simulation perfectly reproduced the three distinct bands in the spectrogram. Also, the growth rates of the unstable MTM modes are shown in blue pluses.

frequencies, f in kHz, and growth-rates, γ (c_s/ρ_s), of the global linear modes are shown in Fig. (6). The orange bands correspond to the frequencies of the magnetic fluctuations in the spectrogram (Fig. 1). Notably, the frequencies of the unstable MTM find a near-quantitative correspondence with the bands in the spectrogram. The low modes ($n = 3, 5, 6$) all have frequencies that are at the high range (or perhaps slightly above) the observed frequency bands. In this context, we make two comments. First, the most relevant range for this comparison is indeed the highest end of the frequency

ranges, since the simulations are based on the profiles at the end of the ELM cycle. Second, Refs. 12 and 13 also note that the linear modes produce frequencies slightly above the fluctuation bands but demonstrate a nonlinear reduction of the frequency due to local flattening (i.e. reduction of local ω_*) of the background electron temperature profile.

Perhaps most strikingly, the simulation results agree closely with the distinctive low frequency band structure, with unstable modes at $n = 3, 5, 6$ and a gap corresponding to the stable mode at $n = 4$. Recall from Sec. II that the lowest frequency band is identified as $n = 3$ in the fluctuation data, in agreement with these simulations. The physical mechanism underlying this band gap has been alluded to above in Sec. III, namely the requirement for rational surfaces to align with the peak in the ω_* profile.

Fig. 7 shows several important physical components for understanding this behavior. Two dimensional wavefunctions of the MTMs for selected toroidal mode numbers ($n = 3, 4, 5$) are plotted in the upper panel. The lower panel shows the same wavefunctions decomposed into their constituent poloidal mode numbers, m , along with the radial profile of ω_* . The relevant rational surfaces are plotted as vertical lines. The modes peak at the rational surfaces that lie closest to the peak value of ω_* .

If the rational surface for a given n number aligns with the peak of the diamagnetic frequency, then a MTM at that toroidal mode number is found to be unstable. Recall from Fig. 6 that the $n = 3$ and $n = 5$ MTMs are unstable, while the $n = 4$ eigenmode is stable and note the relative alignment of these modes with the peak in ω_* shown in Fig. 7. This same behavior is described for a JET discharge in Ref. 13 demonstrated by extensive variations in the q profile and explored in depth using a simplified model in Ref. [29].

We note also the difference between the local and global approaches for the bands below 120 kHz, where the MTMs from local simulations produce unstable modes at each consecutive toroidal mode number and don't exhibit the band gap. The reason is simple: the local approximation knows nothing about the ω_* profile, which is, rather, characterized by a single value representing the local gradients.

The eigenmodes in the upper band $n_\phi = 16 - 29$ (not shown here) also align with the peak in the ω_* profile. However, since the higher n rational surfaces are more dense, the considerations of profile alignment do not pertain. Consequently, the modes are unstable at each consecutive toroidal mode number in the upper band. The question remains, however, of the distinction between the lower MTM range and the higher range, which will be addressed in the next section.

V. SLAB AND TOROIDAL MTM

Having elucidated the origin of the distinctive low- n band structure, we turn our attention now to the physical mechanism underlying the higher n band of MTM. Already in Figs. 4 and 5, we have noted distinctions in the transport signatures of the two bands. Further insights can be gained by considering

the collisionality dependence, the variation with ballooning angle, and the contributions of various terms to the instability drive.

A. Scanning Collision Frequency

Collision dependence of growth rates from global linear simulations is shown in Fig. 8 for three representative toroidal mode numbers, $n=3, 5$, and 19. All unstable modes shown in Fig. (8) are identified as MTMs based on the transport and flux ratios discussed in section(IV A and IV A). At $n=3$ and 5, the MTMs are stable at both low and high collision frequencies with the ratio of the nominal collision frequencies (in red circles) to the corresponding MTM frequencies of order unity, consistent with the conventional picture of the slab MTM (Refs. 1 and 12). In contrast, the MTMs in the upper band ($n = 19$ shown in Fig. 8) exhibit a second branch in the low-collisionality limit, where the experiment lies, suggesting additional physics contributing to the instability. At the experimental point, the ratio of the nominal collision frequency to the corresponding MTM frequency is much smaller than unity.

B. Scanning Ballooning Angle

For further understanding of the nature of the MTM instabilities at the low and high bands a ballooning angle scan is done at $n=3$ and 22 for the local linear simulations. The growth rates and frequencies in Fig. 9 are found to be independent of the ballooning angle at $n = 3$, however, they peak at a finite value of the ballooning angle for $n = 22$. Thus, the MTMs in the upper band depend sensitively on the details of the toroidal geometry. Further investigation identifies substantial contributions of both the curvature term as well as trapped particles to the instability drive. Additional details of this MTM branch will be described in a future publication.

C. Scanning Electron Temperature Gradient

Thus far we have demonstrated a close connection between the MTM frequencies and the observed fluctuation bands. The question remains whether the MTM limits the pedestal temperature in a meaningful way. To address this, we show a scan of the electron temperature gradient (a/L_{Te}) around the nominal values in Fig. 10. The scan is done at $\pm 10\%$ and $\pm 20\%$ of the nominal value of L_{Te} (without reconstructing a self-consistent equilibrium) at $\rho_\phi = 0.975$ at three selected mode numbers in the three bands found in the magnetic spectrogram, $n_\phi = 3, 5$, and 22, and the growth rates and frequencies are shown in Fig. 10.

As expected, the growth rates increase with temperature gradient. The $n = 5$ mode retains a substantial growth rate even at the lowest gradient. Notably, the $n=3$ and 22 modes are quite near their respective instability thresholds at the experimental point. The dependence of the $n = 22$ mode is par-

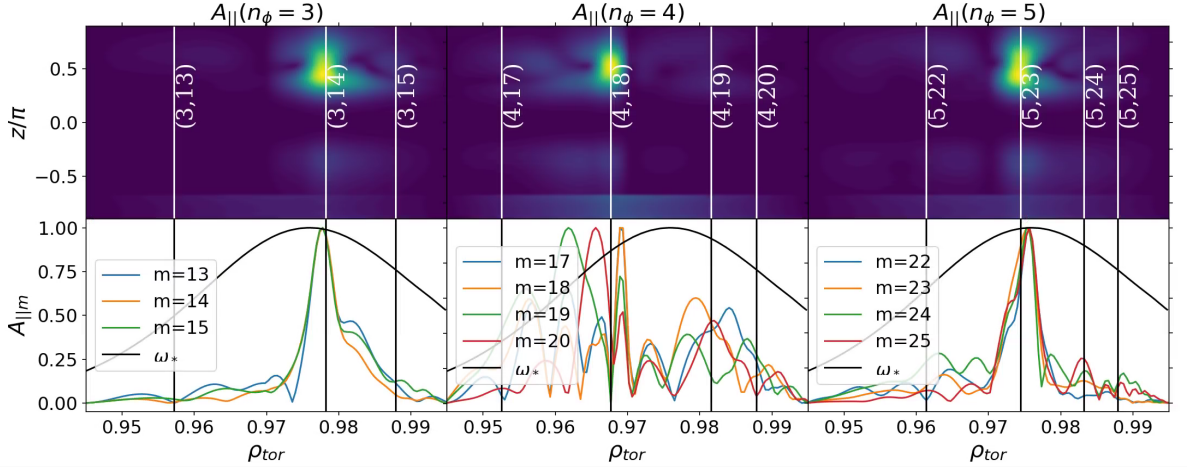


FIG. 7. Samples of the global mode structures for MTMs at the lower ($n_\phi = 3 - 5$) band. The top part of each subplot is the 2-D structure of the mode, however the lower part shows the mode structure decomposed in poloidal harmonics at each toroidal number along with the diamagnetic frequency (ω^*) profile with both normalized to the maximum value. The alignment of the peak of the MTMs with ω_{max}^* indicates a possibility of unstable MTM mode. However if the peak of the mode structure is far away from ω_{max}^* like in $n_\phi = 4$ case, the MTM is stable.

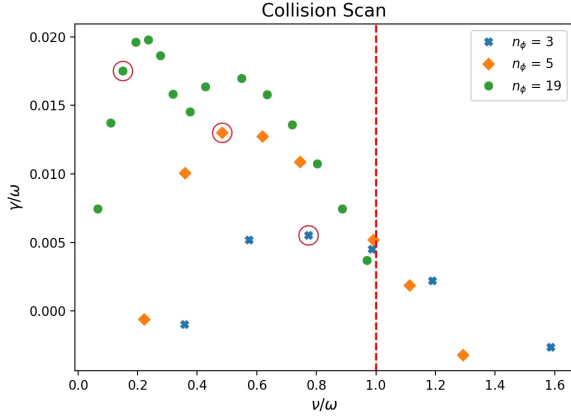


FIG. 8. A series of global linear simulations to scan a range of collision frequencies at $n_\phi = 3, 5$, and 19 . These scans show that the MTM modes at the lower bands are collisional modes with slab characteristics, however, the modes at the higher band are collisionless modes with toroidal characteristics. The red circles refers to the nominal collision frequency.

ticularly strong as the gradient increases. These results are consistent with the notion that the MTM constrains the electron temperature gradient in the pedestal. This is also reinforced by the nonlinear simulations described below.

VI. LOCAL NONLINEAR SIMULATIONS

The main results of the paper are described above: (1) the close agreement between the linear MTM frequencies and the observed frequency bands, and (2) a clear physical explanation for the distinctive band structure. As a consequence of the intrinsically global nature of the MTMs, described above,

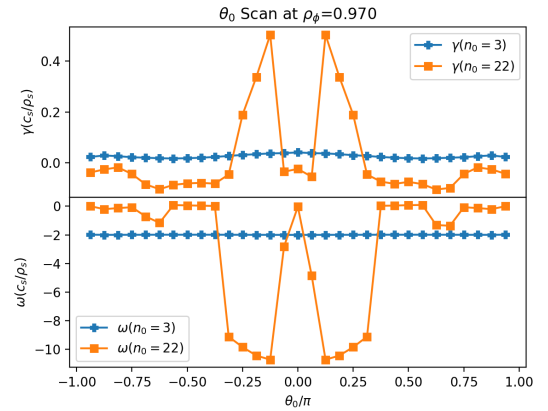


FIG. 9. A ballooning angle scan at selected mode numbers in the low ($n = 3$) and high ($n = 22$) bands. The growth rates do not vary with θ_0 in the low band but they peak at a finite θ_0 in the high band. This is a clear signature of the distinction between slab and curvature driven MTM modes.

global nonlinear simulations would be desirable. Recent developments in GENE code have enabled more robust nonlinear global simulations of strongly electromagnetic modes. Such simulations for this pedestal scenario are currently under investigation and will be reported elsewhere. Here we describe local nonlinear simulations at $\rho_{tor} = 0.975$ with a somewhat idealized setup and probe the sensitivity of the simulations to $E \times B$ shear.

We investigate simulations employing an adiabatic ion approximation. This simplifies the system by eliminating most instabilities except MTM and ETG. For these modes, the modifications are quantitative but not qualitative. The simulations employ grid resolution $n_x = 128$ (spanning negative and positive wavenumbers), $n_{k_y} = 40$ (spanning $k_y > 0$ wavenumbers),

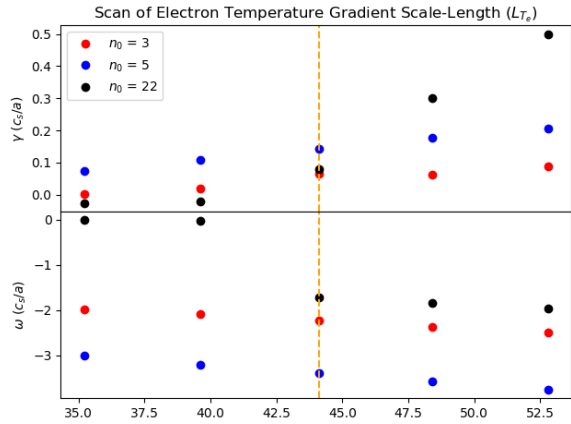


FIG. 10. The growth rates and frequencies of a scan over L_{Te} at selected mode numbers, $n = 3, 5,$ and 22 . Dashed vertical orange line is at the nominal L_{Te} .

$n_z = 128$, $n_v = 36$, and $n_w = 16$. The simulation box extends in the x -axis for $l_x \rho_s = 91.1646$ and has a minimum wavenumber of $k_y \rho_s = 0.018$ in the y -direction. We carry out two simulations: one with zero $E \times B$ shear rate and another with $\gamma_{ExB} = -0.671$.

The time trace of the heat flux for the simulations of the no-shear and full-shear flows are shown in the lower panels of Figs. 11 and 12, respectively. In Fig. 11, two distinct saturation phases are observed: an initial phase $t(c_s/a) = 50 - 90$ followed by a gradual transition to a much higher saturation level after $t(c_s/a) = 150$. Several features of the early saturation phase compare favorably with the experiment. In this phase, the transport level is 1.2 MW compared with expected ~ 1.5 MW of electron thermal transport reported in Ref. 35. However, including the full shear flow in the nonlinear simulation dramatically reduced the heat transport in the saturation phase - compared to that of the no-shear flow case - to be around 0.75 MW (Fig.12). Nonlinear simulations of ETG turbulence predict between 0 and 1 MW of transport (Ref. 35 and 36), so both the early and final saturation phases of the MTM simulation in the no-shear and full-shear cases, respectively, are in a reasonable range in comparison with experimental expectations. It is likely that MTM and ETG interact to account for the electron heat transport in this discharge (see Ref. 5, 13, and 37 for a discussion of such interaction).

In addition to the transport level, the time-average spectrum of the electromagnetic (Q_{em}/Q_{GB}) heat flux reflects the linear eigenvalue spectrum, which, in turn corresponds to the magnetic fluctuations as described above. The upper panel of Fig. 11 shows two distinct bands similar to the lower (slab MTM) and upper (curvature-driven MTM) bands of MTM instabilities in the local linear simulations. In the upper panel of Fig. 12, however, the upper band weakened in the transition phase $t(c_s/a) = 410 - 510$ before acquiring part of its energy back over the saturation phase $t(c_s/a) = 510 - 710$, and we can observe the presence the three peaks that are found experimentally. The peak of spectrum at the lower and upper bands should reflect the relative magnitude of the growth rates in

the linear spectrum. In the spectrogram, however, the upper band appears weaker than the lower band. This is likely due to the more rapid falloff of high m fluctuations as they propagate outside the plasma to the location of the magnetic pickup coils.

The early-time saturation phase of the no-shear flow simulation ($t(c_s/a) = 50 - 90$) does not persist. The later saturation phase is characterized by a condensation of fluctuations to the low k_y wavenumber range as shown in Fig. 11. This does not agree with the multiple bands observed in the fluctuation data. Moreover, the heat flux is ~ 4 MW, which is substantially beyond the experimental expectation. The fluctuations during this later time period are characterized by large radial structures at low k_y .

Inclusion of shear flow limits the growth of the low- k unstable modes and makes them saturate at a lower level. This emphasizes the role that the shear flow plays limiting the heat flux of the unstable MTM modes beside suppressing ITG/TEM modes. The heat flux for this simulation saturates nearer to the experimental expectation (~ 0.75 MW). Moreover, the spectrum retains substantial transport in both the range of low- k_y slab MTM and the higher k_y curvature driven range.

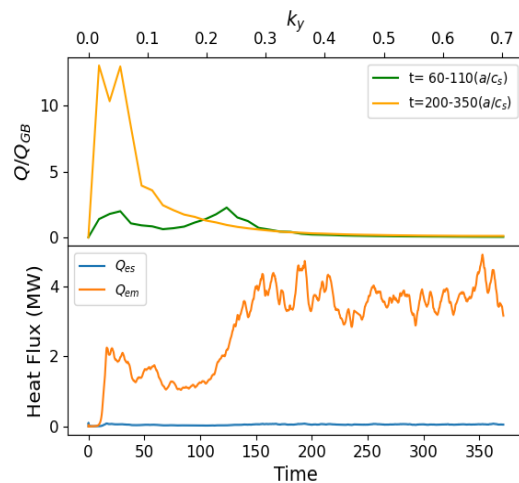


FIG. 11. Time-averaged spectrum of electromagnetic heat flux (Q/Q_{GB}) (Upper-Panel) and time-trace of electrons heat fluxes (Lower-Panel) from a local nonlinear simulation of adiabatic ions without ExB shear flow.

VII. CONCLUSIONS

This paper reports on analysis via gyrokinetic simulations of the magnetic fluctuations in the pedestal of DIII-D discharge #162940. Gyrokinetic simulations find unstable MTMs with frequencies in quantitative agreement with the magnetic spectrogram. Subsequent analysis provides a clear physical explanation for the distinctive band structure.

Three fluctuation bands are observed in the spectrogram: two narrow bands at lower frequency ($f = 35 - 55$ kHz and $f = 70 - 105$ kHz) and a broad band at higher frequency ($f =$

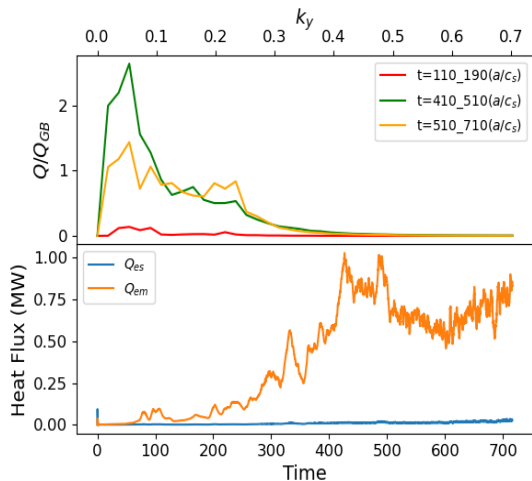


FIG. 12. Time-averaged spectrum of electromagnetic heat flux (Q/Q_{GB}) over different period of times (Upper-Panel) and time-trace of electrons heat fluxes (Lower-Panel) from a local nonlinear simulation of adiabatic ions with ExB shear flow.

300 – 500kHz). The two bands at lower frequency and lower n correspond to slab MTMs with $\omega \sim \omega_* \sim v$. The mode structures are centered at the peak of the ω^* profile and the modes are only unstable when this peak aligns with a rational surface. This property explains the band gap observed in the lower frequency fluctuations, since the $n = 4$ mode does not have a rational surface that aligns with the peak in ω^* . While local simulations qualitatively capture the MTM instability in this range, a global treatment was necessary to describe the sensitive n number selection and consequent band gaps in the spectrum.

At higher wave numbers and higher frequencies, the MTMs are sensitive to the details of the toroidal geometry and depend on curvature drive. The frequency range of these MTMs agrees quantitatively with a high frequency band in the spectrogram. Due to the closely packed rational surfaces at high n , the modes are unstable for all mode numbers in this range. Collisionality scans demonstrate that the instability persists in a collisionality range below that of the slab branch.

Although the major impact of this work is the clear explanation of the distinctive frequency spectrum, we also report on local nonlinear simulations. We note the sensitivity of MTM saturation level to $E \times B$ shear. Without shear, the simulation evolves from an early saturation phase with a reasonable level of heat transport to a later saturation phase where the transport condenses to low wavenumbers and high transport levels. The full-shear simulation exhibits a saturation period with realistic transport levels and multiple peaks corresponding to the slab and curvature branches. Ongoing nonlinear global simulations will be presented elsewhere, including kinetic ions and impurity effects.

Altogether, this work clearly demonstrates that (i) gyroki-

netic simulations are capable of quantitatively capturing many aspects of an important pedestal fluctuation, (ii) basic theoretical considerations can explain the distinctive features of experimentally observed frequency spectra, and (iii) MTMs are unambiguously active and likely responsible for a substantial amount of the anomalous electron transport in the pedestal of this discharge. In combination with other work 11–13, and 18, this further establishes the MTM as a prominent fluctuation in the H-mode pedestal.

VIII. ACKNOWLEDGEMENTS

Ehab Hassan and David Hatch are supported by the SciDAC Center PARTNERSHIP CENTER FOR HIGH-FIDELITY BOUNDARY PLASMA SIMULATION (HBPS) under Award No: DE-SC0018148. David Hatch was also supported by U.S. DOE Contract No. DE-FG02-04ER54742.

This material is based upon work supported by the U.S. Department of Energy, Office of Science, Office of Fusion Energy Sciences, using the DIII-D National Fusion Facility, a DOE Office of Science user facility, under Award(s) DE-FC02-04ER54698, DE-FG02-97ER54415, and DE-AC02-09CH11466.

This research used resources of the National Energy Research Scientific Computing Center (NERSC), a U.S. Department of Energy Office of Science User Facility operated under Contract No. DE-AC02-05CH11231.

The authors acknowledge the Texas Advanced Computing Center (TACC) at The University of Texas at Austin for providing HPC resources that have contributed to the research results reported within this paper.

IX. DATA AVAILABILITY

Simulation data that support the findings of this study are available from the corresponding author upon reasonable request and the approval of coauthors and collaborators.

Disclaimer: This report was prepared as an account of work sponsored by an agency of the United States Government. Neither the United States Government nor any agency thereof, nor any of their employees, makes any warranty, express or implied, or assumes any legal liability or responsibility for the accuracy, completeness, or usefulness of any information, apparatus, product, or process disclosed, or represents that its use would not infringe privately owned rights. Reference herein to any specific commercial product, process, or service by trade name, trademark, manufacturer, or otherwise does not necessarily constitute or imply its endorsement, recommendation, or favoring by the United States Government or any agency thereof. The views and opinions of authors expressed herein do not necessarily state or reflect those of the United States Government or any agency thereof.

-
- [1] Hazeltine R, Dobrott D, Wang T. Kinetic theory of tearing instability. *The Physics of Fluids*. 1975;18(12):1778–1786.
- [2] Drake J, Lee Y. Kinetic theory of tearing instabilities. *The Physics of Fluids*. 1977;20(8):1341–1353.
- [3] Catto PJ, Rosenbluth M. Trapped electron modifications to tearing modes in the low collision frequency limit. *The Physics of Fluids*. 1981;24(2):243–255.
- [4] Applegate D, Roach C, Connor J, Cowley S, Dorland W, Hastie R, et al. Micro-tearing modes in the mega ampere spherical tokamak. *Plasma Physics and Controlled Fusion*. 2007;49(8):1113.
- [5] Guttenfelder W, Candy J, Kaye S, Nevins W, Wang E, Bell R, et al. Electromagnetic transport from microtearing mode turbulence. *Physical review letters*. 2011;106(15):155004.
- [6] Dickinson D, Roach CM, Saarelma S, Scannell R, Kirk A, Wilson H. Kinetic instabilities that limit β in the edge of a tokamak plasma: a picture of an H-mode pedestal. *Physical review letters*. 2012;108(13):135002.
- [7] Canik J, Guttenfelder W, Maingi R, Osborne T, Kubota S, Ren Y, et al. Edge microstability of NSTX plasmas without and with lithium-coated plasma-facing components. *Nuclear Fusion*. 2013;53(11):113016.
- [8] Chowdhury J, Chen Y, Wan W, Parker SE, Guttenfelder W, Canik J. Particle-in-cell δf gyrokinetic simulations of the microtearing mode. *Physics of Plasmas*. 2016;23(1):012513.
- [9] Doerk H, Jenko F, Püschel M, Hatch D. Gyrokinetic microtearing turbulence. *Physical review letters*. 2011;106(15):155003.
- [10] Doerk H, Jenko F, Görler T, Told D, Püschel M, Hatch D. Gyrokinetic prediction of microtearing turbulence in standard tokamaks. *Physics of Plasmas*. 2012;19(5):055907.
- [11] Hatch D, Kotschenreuther M, Mahajan S, Valanju P, Jenko F, Told D, et al. Microtearing turbulence limiting the JET-ILW pedestal. *Nuclear Fusion*. 2016;56(10):104003.
- [12] Kotschenreuther M, Liu X, Hatch D, Mahajan S, Zheng L, Diallo A, et al. Gyrokinetic analysis and simulation of pedestals to identify the culprits for energy losses using ‘fingerprints’. *Nuclear Fusion*. 2019;59(9):096001.
- [13] Hatch DR, Kotschenreuther M, Mahajan SM, Püschel MJ, Michoski C, Merlo G, et al. Microtearing modes as the source of magnetic fluctuations in the JET pedestal. *Nuclear Fusion*. 2020;.
- [14] Hatch D, Kotschenreuther M, Mahajan S, Halfmoon M, Hassan E, Merlo G, et al. Final Report for the FY19 FES Theory Performance Target. USDOE Office of Science (SC)(United States); 2019.
- [15] Halfmoon MR, Hatch DR, Kotschenreuther MT, Mahajan SM, Nelson AO, Kolemen E, et al. Gyrokinetic analysis of inter-ELM transport mechanisms in DIII-D pedestals. in preparation;.
- [16] Jian X, Holland C, Candy J, Belli E, Chan V, Garofalo AM, et al. Role of Microtearing Turbulence in DIII-D High Bootstrap Current Fraction Plasmas. *Physical Review Letters*. 2019;123(22):225002.
- [17] Chen J, Ding W, Brower D, Finkenthal D, Muscatello C, Tausig D, et al. Faraday-effect polarimeter diagnostic for internal magnetic field fluctuation measurements in DIII-D. *Review of Scientific Instruments*. 2016;87(11):11E108.
- [18] Chen J, Brower D, Ding W, Yan Z, Osborne T, Strait E, et al. Internal measurement of magnetic turbulence in ELMy H-mode tokamak plasmas. *Physics of Plasmas*. 2020;27(12):120701.
- [19] Diallo A, Lagner FM. Turbulence dynamics during the pedestal evolution between edge localized modes in magnetic fusion devices. *Plasma Physics and Controlled Fusion*. 2020;.
- [20] Curie M, Halfmoon MR, Chen J, Hatch DR, Brower DL, Hassan E, et al. Gyrokinetic Simulations Compared with Magnetic Fluctuations Diagnosed with a Faraday-Effect Radial Interferometer-Polarimeter in the DIII-D pedestal. in preparation;.
- [21] Perez C, Koslowski H, Hender T, Smeulders P, Loarte A, Lomas P, et al. Washboard modes as ELM-related events in JET. *Plasma physics and controlled fusion*. 2003;46(1):61.
- [22] Diallo A, Hughes J, Greenwald M, LaBombard B, Davis E, Baek S, et al. Observation of edge instability limiting the pedestal growth in tokamak plasmas. *Physical review letters*. 2014;112(11):115001.
- [23] Diallo A, Groebner R, Rhodes T, Battaglia D, Smith D, Osborne T, et al. Correlations between quasi-coherent fluctuations and the pedestal evolution during the inter-edge localized modes phase on DIII-D. *Physics of Plasmas*. 2015;22(5):056111.
- [24] Lagner F, Wolfrum E, Cavedon M, Mink F, Viezzer E, Dunne M, et al. High frequency magnetic fluctuations correlated with the inter-ELM pedestal evolution in ASDEX Upgrade. *Plasma Physics and Controlled Fusion*. 2016;58(6):065005.
- [25] Cavedon M, Dux R, Pütterich T, Viezzer E, Wolfrum E, Dunne M, et al. On the ion and electron temperature recovery after the ELM-crash at ASDEX Upgrade. *Nuclear Materials and Energy*. 2019;18:275–280.
- [26] Lagner F, Diallo A, Cavedon M, Kolemen E. Inter-ELM pedestal localized fluctuations in tokamaks: Summary of multi-machine observations. *Nuclear Materials and Energy*. 2019;19:479–486.
- [27] Moser A, Casali L, Covele B, Leonard A, McLean A, Shafer M, et al. Separating divertor closure effects on divertor detachment and pedestal shape in DIII-D. *Physics of Plasmas*. 2020;27(3):032506.
- [28] Strait E. Magnetic diagnostic system of the DIII-D tokamak. *Review of scientific instruments*. 2006;77(2):023502.
- [29] Larakers JL, Curie M, Hatch DR, Hazeltine RD, Mahajan SM. Global Theory of Microtearing Modes in the Tokamak Pedestal. *Phys Rev Lett*. 2021 Jun;126:225001. Available from: <https://link.aps.org/doi/10.1103/PhysRevLett.126.225001>.
- [30] Jenko F, Dorland W, Kotschenreuther M, Rogers B. Electron temperature gradient driven turbulence. *Physics of plasmas*. 2000;7(5):1904–1910.
- [31] Goerler T, Lapillonne X, Brunner S, Dannert T, Jenko F, Merz F, et al. The global version of the gyrokinetic turbulence code GENE. *Journal of Computational Physics*. 2011;230(18):7053–7071.
- [32] Jenko F, Dannert T, Angioni C. Heat and particle transport in a tokamak: advances in nonlinear gyrokinetics. *Plasma physics and controlled fusion*. 2005;47(12B):B195.
- [33] Jarema D, Bungartz HJ, Görler T, Jenko F, Neckel T, Told D. Block-structured grids for Eulerian gyrokinetic simulations. *Computer Physics Communications*. 2016;198:105–117.
- [34] Jarema D, Bungartz HJ, Görler T, Jenko F, Neckel T, Told D. Block-structured grids in full velocity space for Eulerian gyrokinetic simulations. *Computer Physics Communications*. 2017;215:49–62.
- [35] Hassan E, Hatch D, Guttenfelder W, Chen Y, Parker S. Gyrokinetic benchmark of the electron temperature-gradient instability

- in the pedestal region. *Physics of Plasmas*. 2021;28(6):062505.
- [36] Guttenfelder W, Groebner RJ, Canik JM, Grierson BA, Belli EA, Candy J. Testing predictions of electron scale turbulent pedestal transport in two DIII-D ELMy H-modes. *Nuclear Fusion*. 2021;.
- [37] Pueschel MJ, Hatch DR, Kotschenreuther M, Ishizawa A, Merlo G. Multi-scale interactions of microtearing turbulence in the tokamak pedestal. *Nucl Fusion*. 2020 Dec;60(12):124005. Available from: <https://iopscience.iop.org/article/10.1088/1741-4326/abba49>.